MIT Open Access Articles

On the Inference of Thermal Inversions in Hot Jupiter Atmospheres

ON THE INFERENCE OF THERMAL INVERSIONS IN HOT JUPITER ATMOSPHERES

N. Madhusudhan[1] AND S. Seager[1,2]
[1] MIT Kavli Institute for Astrophysics and Space Research, and Department of Earth, Atmospheric, and Planetary Sciences, MIT,
Cambridge, MA, 02139, USA; nmadhu@mit.edu
[2] Department of Physics, MIT, Cambridge, MA 02139, USA

ABSTRACT

Several studies in the recent past have inferred the existence of thermal inversions in some transiting hot Jupiter atmospheres. Given the limited data available, the inference of a thermal inversion depends critically on the chemical composition assumed for the atmosphere. In this study, we explore the degeneracies between thermal inversions and molecular abundances in four highly irradiated hot Jupiter atmospheres, dayside observations of which were previously reported to be consistent with thermal inversions based on *Spitzer* photometry. The four systems are HD 209458b, HAT-P-7b, TrES-4, and TrES-2. We model the exoplanet atmospheres using a one-dimensional line-by-line radiative transfer code with parameterized abundances and temperature structure, and with constraints of energy balance and hydrostatic equilibrium. For each system, we explore the model parameter space with $\sim 10^6$ models using a Markov chain Monte Carlo routine. Our results primarily suggest that a thorough exploration of the model parameter space is necessary to identify thermal inversions in hot Jupiter atmospheres. We find that existing observations of TrES-4 and TrES-2 can both be fit very precisely with models with and without thermal inversions, and with a wide range in chemical composition. On the other hand, observations of HD 209458b and HAT-P-7b are better fit with thermal inversions than without, as has been reported previously. Physically plausible non-inversion models of HD 209458b and HAT-P-7b fit the data only at the 1.7σ observational errors; better fits require substantial enhancement of methane and depletion of CO, which seems implausible in the very hot atmospheres considered here. Second, in the sample under consideration here, we do not see a correlation between irradiation levels and thermal inversions, given current data. Before JWST becomes available, near-IR observations from the ground and with the *Hubble Space Telescope*, along with existing *Spitzer* observations, can potentially resolve thermal inversions in some systems. Observations with only two channels of *Warm Spitzer* photometry and good signal-to-noise ratio can likely identify or rule out thermal inversions if the difference between the fluxes in the 3.6 and 4.5 μm channels is very high.

Key words: planetary systems – planets and satellites: general – radiative transfer

Online-only material: color figures

1. INTRODUCTION

Observations of dayside atmospheres of several hot Jupiters have indicated the existence of thermal inversions. The inference of thermal inversions is a result of high signal-to-noise *Spitzer* observations (Knutson et al. 2008; Knutson et al. 2009; Machalek et al. 2009; O'Donovan et al. 2010; Christiansen et al. 2010) and concomitant theoretical modeling (Burrows et al. 2007, 2008; Fortney et al. 2008; Madhusudhan & Seager 2009). Thermal inversions have been reported based on flux excesses in certain *Spitzer* channels. A natural explanation of channel-specific high flux is to invoke molecular emission features, as opposed to absorption features (Burrows et al. 2007, 2008; Fortney et al. 2008). Under the assumption of local thermodynamic equilibrium, molecular emission features form only in the presence of a thermal inversion, a region in the atmosphere where temperature increases outward, as in Earth's stratosphere.

Preceding recent observations, early theoretical work on hot Jupiter atmospheres using self-consistent one-dimensional atmosphere models predicted the existence of thermal inversions based on absorption due to TiO and VO (Hubeny et al. 2003; Fortney et al. 2006). More recently, Fortney et al. 2008 classified hot Jupiters in two categories based on the degree of incident irradiation. The class of atmospheres with very high incident flux, dubbed "very hot Jupiters" or "pM" class, was considered favorable to host thermal inversions caused due to gaseous TiO and VO absorption at low pressures, and atmospheres with lower

fluxes were predicted to be unlikely to host inversions owing to condensation of TiO/VO. The flux boundary for this dichotomy was, somewhat arbitrarily, chosen to be $\sim 10^9$ erg s^{-1} cm^{-2}. However, while inferences of some recent observations have purported to violate this hypothesis (e.g., Machalek et al. 2009), others have found present observations insufficient to test this hypothesis (O'Donovan et al. 2010; Fressin et al. 2010).

The theory behind the absorbers causing thermal inversions in hot Jupiter atmospheres is still under debate; it is discussed in detail in Section 2.1. Recent theoretical studies suggest that TiO/VO may not be able to totally account for the inferred thermal inversions (Spiegel et al. 2009). Other alternatives proposed in recent studies include strong UV/visible absorption due to photochemically produced sulfur compounds (Zahnle et al. 2009) and correlation of thermal inversions with chromospheric activity of host stars (Knutson et al. 2010). Since the nature of the absorbers causing the inversions is not known, models that have been successful in inferring thermal inversions have either adopted a parametric absorber (Burrows et al. 2008), or a parameterized temperature profile (see, e.g., Madhusudhan & Seager 2009).

Existing models inferring thermal inversions rest on several assumptions and parameterization. Models typically invoke several free parameters to induce a thermal inversion in the temperature profile, as suggested by the data. The free parameters range from the location and magnitude of an unknown opacity source (e.g., Burrows et al. 2007, 2008) to parameterizing the

temperature profile itself (e.g., Madhusudhan & Seager 2009). In addition, exoplanet atmosphere models traditionally span only a limited range in chemical abundances, often assuming thermo-chemical equilibrium (Barman et al. 2005; Seager et al. 2005; Fortney et al. 2006; Burrows et al. 2007, 2008). While some reported models require thermal inversions to explain the observations, it is not known if the model parameter space has been thoroughly exhausted. It remains to be seen whether some of the observations can be explained without thermal inversions, if we were to relax many of the assumptions and thoroughly explore the parameter space.

In the present work, our primary goal is to understand the extent to which thermal inversions can be robustly inferred in hot Jupiter atmospheres, with current observations. We choose a test sample of four systems for which *Spitzer* observations in the past have been reported to be consistent with thermal inversions. We then pursue a detailed exploration of the model parameter space to see the extent to which the observations can be explained by models with and without thermal inversions. We accomplish this by computing large ensembles of inversion and non-inversion models ($N \sim 10^6$), exploring the parameter space for best-fitting solutions. For each system, we report quantitatively how well the data can be fit by models with and without thermal inversions and with what ranges in atmospheric chemical composition. This approach also reveals the underlying correlations between the different chemical species and between the composition and temperature structure. In addition, since the systems considered here have different levels of irradiation, we also seek to understand if the presence or absence of thermal inversions is correlated with the degree of irradiation, at the level of current data.

We focus on four hot Jupiters for which existing observations were reported to be consistent with thermal inversions in their dayside atmospheres and for which photometric observations of thermal emission are available in four or more *Spitzer* channels. The planets are HD 209458b, HAT-P-7b, TrES-4, and TrES-2. Burrows et al. (2008) and Knutson et al. (2008) first reported a thermal inversion in HD 209458b, based on *Spitzer* photometry in five channels reported by Knutson et al. (2008) and Deming et al. (2005). Madhusudhan & Seager (2009) confirmed the thermal inversion in HD 209458b, for model fits within the 1.4σ observational uncertainties. Additional observations of HD 209458b are available in the near-IR, obtained with the *Hubble Space Telescope* (*HST*) NICMOS, but were explained by models with and without inversions alike (Swain et al. 2009). Knutson et al. (2009) reported a thermal inversion in TrES-4b based on five-channel *Spitzer* photometry using models based on Burrows et al. (2008). O'Donovan et al. (2010) reported observations of TrES-2 in four *Spitzer* IRAC Channels, which were explained by models with and without thermal inversions; they preferred the inversion model which seemed more favorable amongst the set of models explored in that study. Croll et al. (2010) reported a ground-based detection of TrES-2 in the *Ks* band, and noted that their observation along with the four *Spitzer* observations could be explained equally well by models with and without thermal inversions. More recently, however, Spiegel & Burrows (2010) reported that models assuming radiative and chemical equilibrium cannot explain the *Spitzer* observations of TrES-2 without invoking thermal inversions. Finally, Christiansen et al. (2010) reported a thermal inversion in HAT-P-7b, based on four *Spitzer* IRAC channels, along with an observation in the visible by the *Kepler Space Telescope* (Borucki et al. 2009). While the *Kepler* point was not necessarily

decisive in constraining the thermal inversion itself, it allowed constraints on the albedo, day–night redistribution and the TiO/VO abundance. Spiegel & Burrows (2010) confirmed the presence of a thermal inversion in HAT-P-7b using the observations of Christiansen et al. (2010).

The observations of TrES-2 and HAT-P-7b noted above were first interpreted using the exoplanet atmosphere model developed in Madhusudhan & Seager (2009), which is also used in the present work. In both those studies, i.e., of O'Donovan et al. (2010) and Christiansen et al. (2010), we had reported a representative set of models which explained the data. In the present study, we report a more exhaustive exploration of the model parameter space for these systems using a new parameter space exploration scheme described in Section 3.2.

We discuss the theoretical and observational basis of thermal inversions in Section 2. We explain the model framework in Section 3, along with the parameter exploration method and the selection of systems for our study. In Section 4, we present our results, followed by a summary and discussion in Section 5.

2. THERMAL INVERSIONS IN HOT JUPITER ATMOSPHERES

Several arguments have been proposed in the literature justifying the existence of thermal inversions in some hot Jupiter atmospheres. Compelling *Spitzer* IRAC observations of some hot Jupiters suggest that anomalies in the form of planet–star flux excess in some channels cannot be explained without invoking thermal inversions (Burrows et al. 2007; Knutson et al. 2008; Madhusudhan & Seager 2009; Swain et al. 2009). However, it is not known whether such an inference is an outcome of the model input choices used to infer the observations. On the other hand, independent of observations, several theoretical arguments support the existence of thermal inversions in some hot Jupiter atmospheres (Hubeny et al. 2003; Burrows et al. 2007; Fortney et al. 2008).

In this section, we explore the arguments in favor of thermal inversions and motivate the framework under which they can be tested. We begin with the theoretical motivation for thermal inversions, followed by arguments leading to inference of thermal inversions from observations. We then pose the question of whether the observations can be explained without thermal inversions if some of the model constraints are relaxed. Finally, we set up the framework in which the requirement of thermal inversions can be robustly tested.

2.1. Theoretical Basis for Thermal Inversions

Thermal inversions are a natural consequence of visible/UV absorption of incident star light high in the atmosphere. For an isolated planetary atmosphere in hydrostatic equilibrium, and no local energy sources, the atmospheric temperature decreases with pressure (i.e., with increasing distance from center); the atmosphere is heated from below and cools monotonically outward. However, in planetary atmospheres irradiated by the host star, strong optical/UV absorbers in the higher layers of the atmosphere can intercept part of the incident star light. Such local deposition of energy results in a zone in the planetary atmosphere where temperature increases outward, i.e., a "thermal inversion." Most solar system planets have thermal inversions in their atmospheres. In Earth's atmosphere, for example, a thermal inversion is caused by ozone (O_3), which is a strong absorber in the UV (Chamberlain 1978). And, in Jupiter's
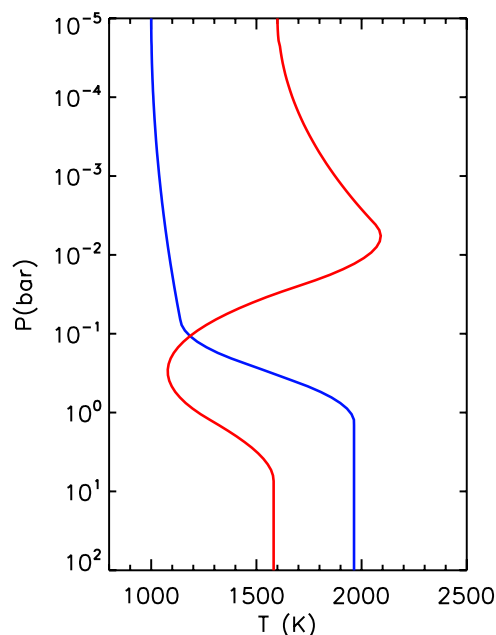
Figure 1. Illustration of *P–T* profiles. The red and blue curves show *P–T* profiles with and without a thermal inversion, respectively. The molecular features due to each of these profiles are shown in Figure 2.

(A color version of this figure is available in the online journal.)

atmosphere, a thermal inversion is caused by strong absorption in the visible by haze resulting from methane photochemistry.

The thermal inversion causing absorbers of solar system planet atmospheres do not survive the temperatures of hot Jupiters. Nevertheless, it has been proposed that thermal inversions could be formed in the atmospheres of very hot Jupiters due to strong absorption of incident stellar radiation in the visible by gaseous TiO and VO (Hubeny et al. 2003; Burrows et al. 2007; Fortney et al. 2008). However, Spiegel et al. (2009) suggested that at mbar pressures where thermal inversions are required to explain the observations, TiO and VO may not be abundant in the required amounts. TiO, being a heavy species, requires a substantial amount of vertical mixing to keep it aloft; the K_{zz} required is 10^7–10^{11} cm^2 s^{-1}, for 0.1–10 μm condensate size, if a cold trap is present. Since neither the particle sizes nor K_{zz} are known, it is uncertain if TiO might be able to explain thermal inversions, and VO is unlikely to help owing to its lower (solar) abundance and lower visible absorption compared to TiO (Spiegel et al. 2009). Zahnle et al. (2009) reported that photochemically produced sulfur compounds, HS and S_2, could have high UV and visible opacities at the temperatures relevant to hot Jupiter atmospheres, making them potential candidates for causing thermal inversions in hot Jupiters. More recently, Knutson et al. (2010) suggested that the presence of a thermal inversion could be inversely correlated with the activity level of the host star, UV flux from the more active stars potentially destroying inversion-causing absorbers. Despite the continuing debate on the inversion-causing absorbers in hot Jupiter atmospheres, thermal inversions have been invoked typically by either adopting a parametric opacity source of unknown nature (Burrows et al. 2008), or by parameterizing the temperature profile (see, e.g., Madhusudhan & Seager 2009).

2.2. Review of Observational Inference of Thermal Inversions

The inferences of thermal inversions are motivated by observations of dayside atmospheres of transiting hot Jupiters using

Spitzer photometry. Observations of some hot Jupiters indicate excess emission in some *Spitzer* channels over others. For example, in the four IRAC observations of HD 209458b reported by Knutson et al. (2008), there is indication of excess emission in the 4.5 μm and 5.8 μm channels. The observations show a markedly higher planet–star flux ratio in the 4.5 μm channel compared to the neighboring 3.6 μm channel, and the flux ratio in the 5.8 μm channel is higher than that in the adjacent channels at 4.5 μm and 8 μm.

The thermal emission spectrum of a planet is influenced by a combination of the atmospheric temperature structure and molecular absorption. Let us consider a hypothetical hot Jupiter atmosphere with the stellar and planetary properties of HD 209458b, and consisting of gaseous H_2O, CO, CH_4, and CO_2, at nominal mixing ratios, close to assumption of chemical equilibrium at solar abundances. In this particular case, we assume that the molecular species are all well mixed in the atmosphere, i.e., uniform volume mixing ratios over the whole atmosphere. Figure 2 shows the spectral features of each of the molecules in such an atmosphere, for *P–T* profiles with and without a thermal inversion (shown in Figure 1). The assumed mixing ratios of the molecules are $H_2O = 10^{-4}$, CO = 10^{-3}, $CH_4 = 10^{-5}$, and $CO_2 = 5 \times 10^{-7}$. As is demonstrated in Figure 2, the atmosphere with a thermal inversion gives rise to molecular emission features, whereas the one without a thermal inversion has absorption features.

The excess emission in some *Spitzer* channels over others can be qualitatively explained by a thermal inversion along with some key molecular features. As can be seen from Figure 2, H_2O has several spectral features in the 3.6 μm, 5.8 μm, 8 μm, 16 μm, and 24 μm *Spitzer* channels. CH_4 has strong features almost exclusively in the 3.6 μm and 8 μm channels. CO has a strong feature in the 4.5 μm channel, also contributing to the 5.8 μm channel. Finally, CO_2 has strong features in the 4.5 μm and 16 μm channels. The 4.5 μm feature of CO_2 is degenerate with the contribution of CO in the same channel. The high fluxes in the 4.5 μm and 5.8 μm channels, as seen in HD 209458b for example, can therefore be explained simply by having strong emission due to CO and CO_2, and only moderate emission due to CH_4 and H_2O (Madhusudhan & Seager 2009). Since emission features can form only due to a thermal inversion, the observations can be interpreted as suggesting the presence of a thermal inversion along with CO and/or CO_2.

The molecular species required to explain the observations are physically plausible. In chemical equilibrium (Burrows & Sharp 1999), CO occurs naturally in the temperature range of HD 209458b (see *P–T* profiles in Burrows et al. 2008; Madhusudhan & Seager 2009; Swain et al. 2009). In addition, CO_2 mixing ratios up to $\sim 10^{-6}$ are allowed by equilibrium chemistry and/or photochemistry (Liang et al. 2003; Zahnle et al. 2009). More generally, hot Jupiters for which thermal inversions are predicted, are characterized by their very hot dayside atmospheres (Fortney et al. 2008), suggesting that dominant contribution to the emergent spectra is expected from CO (Burrows & Sharp 1999).

Care must be exercised while exploring the space of atmospheric composition in order to fit the data. Since a high flux in the 4.5 μm channel can be explained by CO and/or CO_2, it is possible for a fitting model to infer the lack of CO in the atmosphere, by allowing an implausibly high CO_2. Such a proposition would likely be implausible given the hot temperatures where CO is expected to be the dominant form of carbon. The degeneracy between CO and CO_2 can be broken by fitting the model
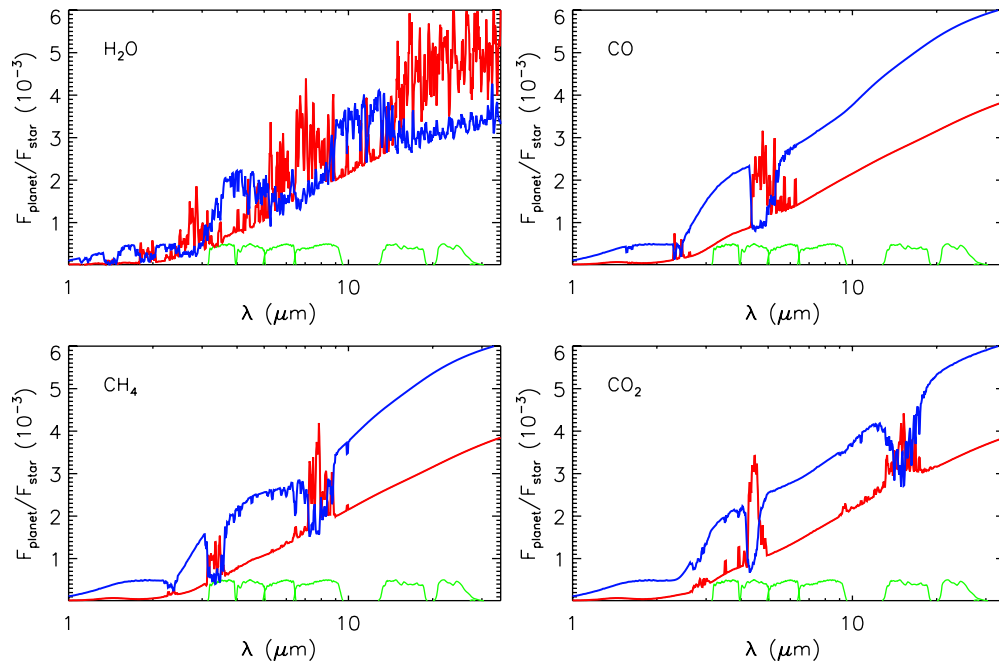
Figure 2. Illustration of molecular features. Each panel shows molecular line features due to a single molecule in a hypothetical atmosphere. The stellar and planetary properties are assumed to be those of the HD 209458b system. The blue curves show the spectral features of an atmosphere without a thermal inversion and red curves show features of an atmosphere with a thermal inversion. The corresponding P–T profiles are shown in Figure 1. The mixing ratios, with respect to H_2, in the four panels are assumed to be $H_2O = 10^{-4}$, $CO = 10^{-3}$, $CH_4 = 10^{-5}$, and $CO_2 = 5 \times 10^{-7}$. The continuum in each spectrum is of the blackbody of the bottom of the atmosphere with features due to H_2–H_2 collision induced opacities. The green curves show the six *Spitzer* band passes at 3.6, 4.5, 5.8, 8, 16, and 24 μm.

(A color version of this figure is available in the online journal.)

to the 16 μm *Spitzer* Infrared Spectrograph (IRS) photometry, where available. The 16 μm channel has dominant contribution due to a strong feature of CO_2 alone. For example, an observation of HD 209458b in the 16 μm channel by D. Deming (2009, private communication) was used in Madhusudhan & Seager (2009) to place simultaneous constraints on CO and CO_2. The same observation is also used in the present work.

2.3. Alternate Qualitative Interpretation

Is there any conceivable scenario, independent of existing models in which the observations can be explained without thermal inversions? A few qualitative alternatives seem feasible. Let us re-consider the situation explained in Section 2.2, where the fluxes in the 4.5 μm and 5.8 μm IRAC channels are higher than those in the 3.6 μm and 8 μm channels, respectively. Let us now investigate if we can explain the same observations with a planet atmosphere which has no thermal inversion (the blue model in Figures 1 and 2). In this case, instead of considering the emission features in the 4.5 μm and 5.8 μm channels, one can consider the absorption features in the 3.6 μm and 8 μm channels, to explain the same flux differential between adjacent channels. The fitting model would then require strong absorption features in the 3.6 μm and 8 μm channels, and weaker absorption in the 4.5 μm and 5.8 μm channels. One conceivable solution is provided by methane (CH_4) which has strong absorption features only in the 3.6 μm and 8 μm channels. So, in principle, a high contribution due to CH_4, over CO or CO_2, could provide the required absorption signatures. Although H_2O also has features in the 8 μm channel, a high abundance of it may not be desirable since it would lead to absorption in the 5.8 μm channel. In presenting this solution, we have exploited the degeneracy between the presence or absence of a thermal inversion and complementary molecular features.

Despite our simple qualitative explanation of a non-thermal-inversion fit to observations like those of HD 209458b, whether or not a model without inversion fits the data, and is physically plausible, is subject to further tests. First, CH_4 has stronger absorption in the 8 μm channel than in the 3.6 μm channel. In other words, for the same molecular composition of CH_4, the absorption in the 8 μm channel with respect to the 5.8 μm channel can be deeper than the absorption in the 3.6 μm channel with respect to the 4.5 μm channel. This is contrary to what is required by the IRAC observations of HD 209458b (Knutson et al. 2008).

A fitting model without a thermal inversion must also satisfy the constraint of energy balance. Explaining the high flux in the 4.5 μm channel with a non-thermal inversion model means that the blackbody continuum of the spectrum must be at the level of the 4.5 μm point or higher. While such a high emergent flux balances the incident stellar flux remains to be verified. Therefore, it is not certain that a non-inversion configuration which fits the data necessarily satisfies the fundamental constraint of energy balance. This latter point could, in principle, be obviated by P–T profiles steep enough to produce deep spectral features in most parts of the spectrum except in the 4.5 μm and 5.8 μm channels. Finally, even if the model fits and maintains energy balance, it is not clear how such extremely hot atmospheres can be dominated by CH_4 over CO. Future theoretical work might explain this possibility.

2.4. A Test for Thermal Inversions

A rigorous inference of thermal inversions from a given set of observations would involve running a large population of models thoroughly exploring the parameter space in search of non-inversion models that fit the data. Not finding a statistically significant fit in such an exploration would constitute strong evidence in favor of thermal inversions from the data set in

question. In a recent work, we demonstrated the capability of running $\sim 10^7$ one-dimensional models on a parameter grid with manageable computational resources (Madhusudhan & Seager 2009). In the same study, we had explored models on predetermined grids in the parameter space of models for HD 189733b and HD 209458b. We were then able to constrain the extent of possible thermal inversions in HD 209458b that fit the *Spitzer* broadband photometry. Such a capability was possible because of the efficient parameterization of the model temperature structure and molecular abundances.

In this study, we combine the model developed in Madhusudhan & Seager (2009) with an efficient parameter space exploration procedure to test the requirement of thermal inversions for a select sample of hot Jupiters. We consider four hot Jupiters at different levels of irradiation for which observations have been known to be consistent with thermal inversions in their respective atmospheres, and for which *Spitzer* photometry is available in four or more channels. We run $\sim 10^6$ models, with and without thermal inversions, for each planet under consideration, and report goodness-of-fit contours in the space of atmospheric composition and temperature structure. In what follows, we describe our model setup, the optimization algorithm, and the systems considered in this study.

3. MODEL AND METHOD

3.1. Model

Our model atmosphere includes a one-dimensional parametric P–T profile coupled with line-by-line radiative transfer, hydrostatic equilibrium, and the requirement of energy balance at the top of the atmosphere (Madhusudhan & Seager 2009). We consider 100 atmospheric layers in the pressure range between 10^{-5} and 100 bar. The key aspect of our model is the parameterization of the P–T profile and the chemical composition, which allows us to run large ensembles of models, exploring the parameter space, in a computationally efficient manner.

The major difference of our model from traditional atmosphere models is in the treatment of energy balance. Our model requires energy balance at the top of the atmosphere, instead of an iterative scheme to ensure layer-by-layer radiative (or radiative + convective) equilibrium as is done in conventional models. We note that the requirement of layer-by-layer radiative equilibrium in a one-dimensional model is not strictly physical since complex hydrodynamics flows in highly irradiated hot Jupiter atmospheres can alter the temperature structure away from radiative equilibrium (Showman et al. 2009). The global energy balance, e.g., at the top of the atmosphere, however, is a strict requirement. For a given set of model parameters, we require that the net energy output at the top of the atmosphere is less than or equal to the net energy input due to the incident stellar flux; a deficit indicates energy redistributed to the night side. Models where the emergent flux is greater than the incident flux are discarded (see Madhusudhan & Seager 2009). By running a large number of ($\sim 10^7$) models in the parameter space, and discarding those that did not satisfy energy balance, we were left with a population of models that satisfied energy balance.

We parameterize the chemical abundances of the molecular species by considering deviations over chemical equilibrium (explained at length in Madhusudhan & Seager 2009). For each molecule under consideration, we compute its mixing ratio in a layer of the atmosphere by multiplying a parametric factor to the mixing ratio that would be expected under thermochemical equilibrium with solar abundances (TE$_\odot$). The parametric factor

for a given molecule is constant over the entire atmosphere, i.e., the mixing ratio profile of the molecule over the entire atmosphere would be shifted relative to that obtained from TE$_\odot$ by the constant factor. We use this treatment for H_2O, CO, and CH_4. For CO_2, we perturb over a uniform mixing ratio of 10^{-6} (1 ppmv or 10^{-6} is just a reference; it is the approximate mixing ratio of CO_2 expected from TE$_\odot$ and/or photochemistry, for $5 \times$ solar metallicity and $T \sim 2000$ K; Zahnle et al. 2009; Liang et al. 2003). Thus, corresponding to the four prominent molecules, we have four parameters $f_{H_2O}, f_{CO}, f_{CH_4}$, and f_{CO_2}. We reiterate that f_X is not the absolute mixing ratio of "X." It is the ratio between the mixing ratio of "X" and the mixing ratio under TE$_\odot$; except for CO_2, for which it is with respect to 10^{-6}. Our models also include NH_3, fixed at the TE$_\odot$ value, and TiO and VO at solar abundances. Additionally, we include H_2–H_2 collision induced cross sections, which are a source of continuum opacity. Our H_2O, CH_4, CO, and NH_3 molecular line data are from Freedman et al. (2008), and references therein. Our CO_2 data are from R. S. Freedman (2009, private communication) and Rothman et al. (2005), and we obtain the H_2–H_2 collision-induced opacities from Borysow et al. (1997) and Borysow (2002). We use a Kurucz model for the stellar spectrum (Castelli & Kurucz 2004).

In the current work, we have made one significant change to our approach in Madhusudhan & Seager (2009). Previously we had run models on a predetermined grid, chosen based on some model-independent arguments outlined in that work. While we were able to run a large population (tens of millions) of models in that approach, the grid resolution was still coarse and sampled evenly over evidently unnecessary regions of the parameter space. In this approach, we run the models using a more efficient parameter space exploration procedure, allowing us to sample the desired error surfaces at much higher resolution.

3.2. Parameter Space Exploration

Our primary requirement in this work is to be able to explore the model parameter space at fine resolution. Even a single plausible model without thermal inversions, in a million models, would still be evidence against the requirement of thermal inversion by a given set of observations.

We use the Markov chain Monte Carlo (MCMC) method to explore the parameter space of models without thermal inversions. The MCMC method is a Bayesian parameter estimation algorithm which allows the calculation of posterior probability distributions of the model parameters conditional to a given set of observations. An extensive body of the literature exists on the applications of MCMC for parameter estimation (Gilks et al. 1998; Tegmark et al. 2004; Ford 2005). The MCMC method allows an efficient means of exploring the parameter space in search of a global solution, with very fine sampling in the allowed range of parameter values. In this work, however, the observations are always less than the number of parameters, i.e., there is no unique solution. However, it is still possible to explore the parameter space and find contours in the error surface of some measure of fit. We, therefore, use the MCMC method with a Metropolis–Hastings scheme within the Gibbs sampler for fine sampling of the model parameter space.

Our model described in Section 3.1 above has 10 free parameters. Six parameters concern the P–T profile: $T_0, P_1, P_2, P_3, \alpha_1$, and α_2 (Madhusudhan & Seager 2009). And, four parameters correspond to the departures of molecular abundances from the reference abundances described in Section 3.1: $f_{H_2O}, f_{CO}, f_{CH_4}$, and f_{CO_2}.

We define some physically motivated boundaries in the parameter space explored by the Markov chain. We impose the constraint of global energy balance by restricting η to [0.0, 1.0], where, $\eta = (1 - A)(1 - f_r)$ is the ratio of emergent flux output on the day side to incident stellar flux input on the day side, weighted appropriately (Madhusudhan & Seager 2009). Here, A is the Bond albedo and f_r is the day–night energy redistribution. We also impose some nominal boundaries on the temperatures and departures from equilibrium chemistry. We explore a wide range of deviations from chemical equilibrium (Burrows & Sharp 1999), empirically selected so as to be general enough. For models without thermal inversions, we set the boundaries as $-9 < \log(f_{H_2O}) < 9$, $-9 < \log(f_{CO}) < 5$, $-5 < \log(f_{CH_4}) < 10$, $-5 < \log(f_{CO_2}) < 4$. The limits are similar for models with thermal inversions, except the lower boundaries for $\log(f_{H_2O})$ and $\log(f_{CO})$, which are set at -4 and -5, respectively. We report all those models which have the overall elemental C/H and O/H abundances within the broad range of $(10^{-2}–10^2)\times$ solar (Anders & Grevesse 1989; Burrows & Sharp 1999; but cf., Asplund et al. 2005; Allende-Prieto et al. 2002). For the temperature structure, the constraint of no thermal inversion is imposed by requiring that $P_1 \geqslant P_2$. The "fit" parameters for the MCMC are T_0, $\log(P_1)$, $\log(P_2)$, $\log(P_3)$, α_1, α_2, $\log(f_{H_2O})$, $\log(f_{CO})$, $\log(f_{CH_4})$, and $\log(f_{CO_2})$. We consider uniform priors in all the parameters. For each system under consideration, we run one chain of 10^6 links for models with thermal inversion and one for models without thermal inversion. Our parametric P–T profile provides a simple means to demarcate between inversion and non-inversion models. The condition for the P–T profile to have no thermal inversion is $P_2 \leqslant P_1 \leqslant P_3$, and that to have a thermal inversion is $P_1 \leqslant P_2 \leqslant P_3$.

3.3. Quantitative Measure of Fit

Central to our analysis is the definition of what constitutes a "fit" to the data. We can only report to what extent a model fits the data relative to the "observational" uncertainties, i.e., within the 1σ error bars or 1.5σ errors, and so on. Given that the number of broadband observations are typically less than the number of model parameters, we cannot report a formal fit with confidence levels. Nevertheless, we evaluate our models based on the ξ^2 statistic, defined as χ^2/N_{obs} (Madhusudhan & Seager 2009):

$$\xi^2 = \frac{1}{N_{obs}} \sum_{i=1}^{N_{obs}} \left(\frac{f_{i,model} - f_{i,obs}}{\sigma_{i,obs}} \right)^2, \qquad (1)$$

where, $f_{i,model}$ and $f_{i,obs}$ are the model and observed flux ratios, respectively, and $\sigma_{i,obs}$ is the 1σ measurement uncertainty. N_{obs} is the number of observations.

For each system, we report the best value of ξ^2 we find with a non-inversion model. We also present the range in parameter space which fits the observations at different levels of ξ^2, for example, $\xi^2 \leqslant 1$, $\xi^2 \leqslant 2$, or higher, as applicable. In this framework, $\xi^2 \leqslant 1$ means the model fits the observations to within the 1σ error bars on average, and a $\xi^2 \leqslant 2$ means a fit to within $\sqrt{2} = 1.4\sigma$ of the error bars on average, and so on.

4. RESULTS

In this section, we report the constraints on the chemical compositions of the dayside atmospheres of the planets in our study. For each planet, we present the range of composition, temperature structure, and day–night energy redistribution required by the best-fit models with no thermal inversions. We

also present the constraints on the composition and day–night energy redistribution of models with thermal inversions for each system.

4.1. HD 209458b

We consider planet–star flux contrasts of HD 209458b in six channels of *Spitzer* broadband photometry. The data include four IRAC observations reported by Knutson et al. (2008), and observations in the 16 μm IRS channel and the 24 μm MIPS channel, by D. Deming (2009, private communication) and Deming et al. (2005), respectively. We focus on these observations which were reported in the literature as suggestive of a thermal inversion in HD 209458b, especially the four IRAC observations.

Our results indicate that HD 209458b is a likely candidate to host a thermal inversion in its dayside atmosphere. However, whether or not HD 209458b actually has a thermal inversion depends on the level of fit, and the physical plausibility of the fitting models one is willing to consider. Figure 3 shows populations of pressure–temperature (P–T) profiles with no thermal inversions which fit the observations at different levels of ξ^2. The corresponding constraints on the atmospheric composition are shown in Table 1, and the constraints for inversion models are shown in Table 2. Figures 4 and 5 show departures of molecular species from TE$_\odot$, for models of HD 209458b with and without thermal inversions.

The observations require a thermal inversion in the atmosphere of HD 209458b at the $\xi^2 = 2$ level. The best-fitting model with no thermal inversion has a ξ^2 of 2.04, implying a fit at 1.43σ (i.e., $\sqrt{2.04}$) of the observations, on average. And, even at this level of fit, the models show substantial departures from thermochemical equilibrium assuming solar abundances (TE$_\odot$). Figure 4 shows the departures in the mixing ratios of CO and CH$_4$ from TE$_\odot$ at different levels of fit. At the $2.0 < \xi^2 < 2.25$ surface (shown in blue dots for the non-inversion case), it can be seen that non-inversion models of HD 209458b require a depletion of CO of at least 10^{-2} times TE$_\odot$ (the departures shown in Figure 4 are in fraction with respect to TE$_\odot$). This low a mixing ratio of CO can, in principle, be achieved by having similarly low abundances of C and O relative to solar. However, the simultaneous requirement of an overabundance of CH$_4$ is hard to explain. Thus, non-inversion models fitting the observations at the 1.5σ errors seem physically implausible.

The observations can be explained by physically plausible non-inversion models at the $\xi^2 \sim 3$ level, meaning a fit at the 1.7σ observational errors. As shown in Figure 4, the $\xi^2 = 3$ level (region with green dots) allows for non-inversion models which have CO within a factor of $\sim$10 from TE$_\odot$. Such a small factor can potentially be explained either by just having different C/H and O/H abundances or due to non-equilibrium processes (Cooper & Showman 2006; Zahnle et al. 2009; Line et al. 2010; Madhusudhan & Seager 2010).

The observations can be fit to within $\xi^2 = 1$ by models with thermal inversions, as has been demonstrated previously by Madhusudhan & Seager (2009). The molecular mixing ratios for inversion models as constrained by the observations are shown in Table 2. Figures 4 and 5 show the deviations from TE$_\odot$ required by the inversion models. We find that the best-fitting models, within $\xi^2 = 1$, allow compositions with CO and CH$_4$ deviant from TE$_\odot$ by a factor of $\sim$10 and higher. However, if we consider the $\xi^2 = 2$ surface, the observations can be fit with inversion models containing close to TE values of CO and CH$_4$, with C/H and O/H abundances only slightly enhanced over
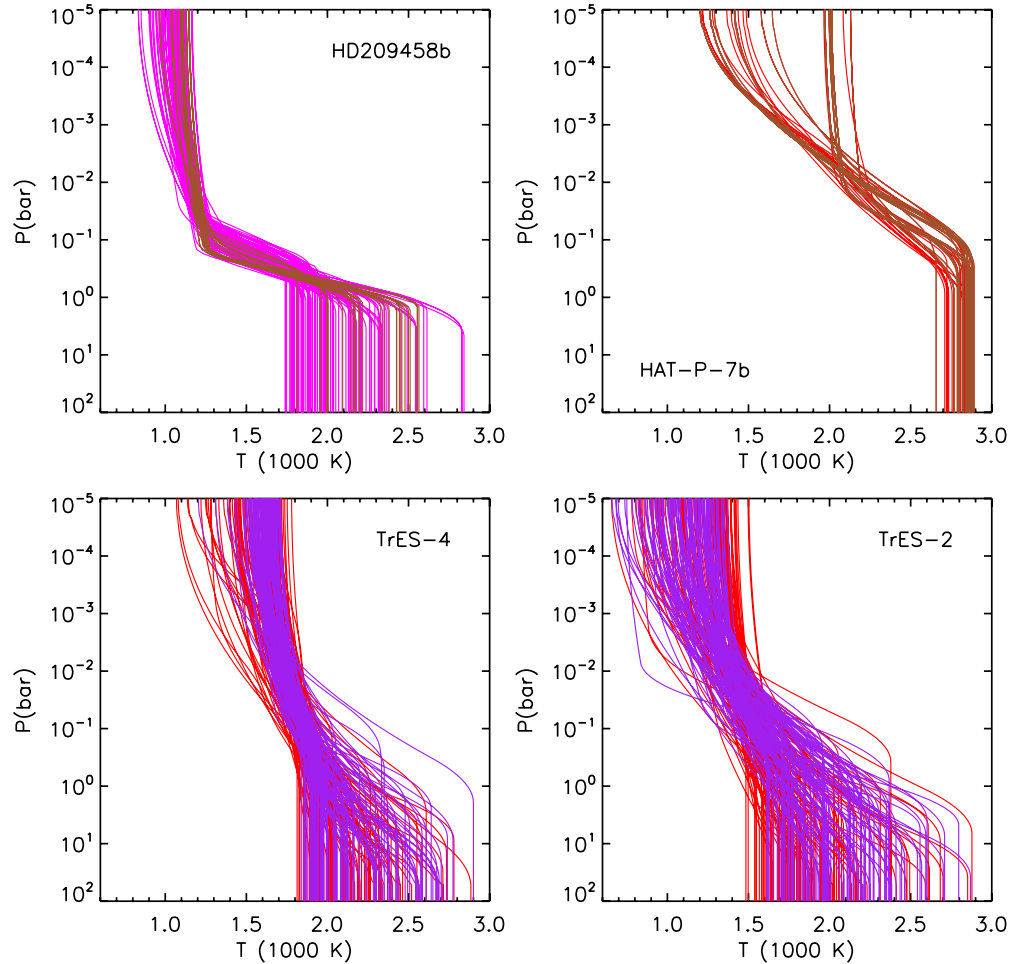
Figure 3. Pressure–temperatures (P–T) profiles for the four systems. Each panel shows the P–T profiles with no thermal inversions that explain the observations at different levels of fit. Best-fitting profiles with thermal inversions for each of these systems have been reported in the literature referred in the text. For HD 209458b, the profiles in magenta correspond to models that fit the observations with $2 < \xi^2 \leqslant 2.25$; the best-fit non-inversion model has $\xi^2 = 2.04$. For HAT-P-7b, the red profiles correspond to models fitting the observations to within $1.6 < \xi^2 \leqslant 2$; the best-fit model had $\xi^2 = 1.65$. The brown profiles for both HD 209458b and HAT-P-7b are 30 profiles that fit best, shown for illustration. For TrES-4 and TrES-2, the red profiles correspond to models that fit within $1 \leqslant \xi^2 \leqslant 2$, and the purple profiles fit to within $\xi^2 < 1$; only 100 randomly chosen profiles from each category are shown, for clarity.

(A color version of this figure is available in the online journal.)

Table 1
Constraints on the Atmospheric Properties for Models Without Thermal Inversions

Quantity	HD 209458b[a]	HAT-P-7b[a]	TrES-4		TrES-2	
	$2 < \xi^2 \leqslant 2.25$	$1.5 < \xi^2 \leqslant 2$	$\xi^2 \leqslant 1$	$\xi^2 \leqslant 2$	$\xi^2 \leqslant 1$	$\xi^2 \leqslant 2$
H_2O[b]	10^{-5}–2×10^{-3}	10^{-12}–2×10^{-5}	10^{-12}–2×10^{-3}	10^{-13}–0.15	8×10^{-6}–0.16	10^{-12}–0.16
CO	10^{-12}–10^{-5}	3×10^{-8}–10^{-4}	10^{-13}–0.06	10^{-13}–0.07	10^{-13}–0.04	10^{-13}–0.07
CH_4	6×10^{-6}–2×10^{-4}	2×10^{-3}–0.05	10^{-15}–0.07	10^{-15}–0.07	10^{-15}–0.07	10^{-15}–0.07
CO_2	10^{-11}–4×10^{-8}	9×10^{-7}–9×10^{-5}	3×10^{-7}–0.02	10^{-12}–0.03	10^{-11}–10^{-5}	10^{-12}–7×10^{-3}
C/O	$0.03 - 0.82$	$15 - 2 \times 10^3$	$0.44 - 4 \times 10^3$	10^{-4}–4×10^3	5×10^{-5}–4×10^3	4×10^{-5}–4×10^3
η[c]	$0.5 - 1.0$	0.7–1.0	$0.37 - 1.0$	$0.33 - 1.0$	$0.36 - 1.0$	$0.29 - 1.0$

Notes.
[a] For HD 209458b and HAT-P-7b, the best-fit non-inversion model has ξ^2 of 2.04 and 1.65, respectively, and hence the reported ranges of ξ^2. See the text for details.
[b] The molecular mixing ratios are quoted as ratios by number with respect to molecular hydrogen.
[c] $\eta = (1 - f_r)(1 - A)$, where, f_r is the day–night redistribution and A is the Bond albedo. $(1-\eta)$ gives the maximum day–night redistribution allowed by the model, i.e., assuming zero albedo.

solar. One potential problem in the inversion scenario, however, is the requirement of low H_2O by the best-fit models. The low observed flux in the 3 μm and 24 μm channels requires low H_2O, which is contrary to the high H_2O requirement imposed by the high observed flux in the 5.8 μm channel. This problem has been previously discussed in the literature (Deming et al. 2005; Seager et al. 2005; Madhusudhan & Seager 2009) and is a subject for future studies.

Table 2
Constraints on the Atmospheric Properties for Models with Thermal Inversions

Quantity	HD 209458b		HAT-P-7b		TrES-4[a]	TrES-2[a]
	$\xi^2 \leqslant 1$	$\xi^2 \leqslant 2$	$\xi^2 \leqslant 1$	$\xi^2 \leqslant 2$	$\xi^2 \leqslant 1$	$\xi^2 \leqslant 1$
H_2O[b]	5×10^{-8}–3×10^{-6}	4×10^{-8}–10^{-5}	10^{-4}–0.16	3×10^{-7}–0.16	5×10^{-8}–0.13	5×10^{-8}–0.16
CO	3×10^{-4}–0.06	3×10^{-4}–0.07	3×10^{-9}–0.07	10^{-9}–0.07	4×10^{-9}–0.07	10^{-9}–0.07
CH_4	9×10^{-4}–0.06	10^{-11}–0.06	10^{-14}–0.07	10^{-15}–0.07	10^{-15}–0.07	10^{-14}–0.07
CO_2	10^{-11}–5×10^{-7}	10^{-12}–8×10^{-7}	10^{-11}–2×10^{-4}	10^{-12}–0.01	10^{-11}–0.02	10^{-11}–0.02
C/O	1–146	1–105	5×10^{-5}–53	5×10^{-5}–207	4×10^{-4}–2×10^3	6×10^{-5}–10^3
η[c]	0.27–0.60	0.25–0.84	0.49–0.83	0.41–0.85	0.36–1.0	0.23–1.0

Notes.
[a] For TrES-2 and TrES-4, the constraints at the $\xi^2 = 2$ level are almost identical to those at the $\xi^2 = 1$ level, and hence we do not report them here.
[b] The molecular mixing ratios are quoted as ratios by number with respect to molecular hydrogen.
[c] $\eta = (1 - f_r)(1 - A)$, where f_r is the day–night redistribution and A is the Bond albedo. ($1-\eta$) gives the maximum day–night redistribution allowed by the model, i.e., assuming zero albedo.

Table 3
Chemical Compositions and Day–night Redistribution of Sample Spectra[a]

System	H_2O	CO	CH_4	CO_2	C/O	η	ξ^2
HD 209458b							
I	6×10^{-06} (0.006)	3×10^{-02} (50)	4×10^{-08} (0.001)	6×10^{-09} (0.006)	1.00	0.38	1.60
NI	4×10^{-05} (0.04)	8×10^{-06} (0.01)	9×10^{-06} (0.8)	5×10^{-11} (5×10^{-05})	0.36	0.56	2.75
HAT-P-7b							
I	7×10^{-03} (7)	6×10^{-04} (0.8)	8×10^{-07} (0.1)	1×10^{-05} (10)	0.07	0.59	0.89
NI	2×10^{-05} (0.02)	5×10^{-04} (0.63)	2×10^{-11} (0.01)	8×10^{-05} (80)	0.85	0.63	3.0
TrES-4							
I	8×10^{-03} (8)	4×10^{-04} (0.6)	5×10^{-08} (1)	2×10^{-08} (0.02)	0.05	0.40	1.76
NI	5×10^{-03} (5)	4×10^{-04} (0.6)	2×10^{-9} (0.2)	2×10^{-05} (23)	0.09	0.41	1.80
TrES-2							
I	2×10^{-03} (2)	1×10^{-03} (2)	1×10^{-05} (0.3)	1×10^{-08} (0.01)	0.44	0.72	0.54
NI	1×10^{-03} (1)	4×10^{-04} (0.6)	2×10^{-08} (0.7)	2×10^{-08} (0.02)	0.23	0.46	0.98

Notes. [a] The two rows for each system correspond to the two model spectra for each system presented in Figure 6. "I" and "NI" correspond to the models with and without a thermal inversion, respectively, in Figure 6. For each molecule, the mixing ratio averaged over all the layers is reported, along with the deviation from TE$_\odot$ shown in parentheses.

Two best-fit model spectra, with and without a thermal inversion, for HD 209458b are shown in Figure 6, along with the *P*–*T* profiles. The corresponding atmospheric composition and day–night redistribution are shown in Table 3. As can be seen from Figure 6, the dominant source of error for the non-inversion model comes from the high flux in the 5.8 μm IRAC observation. While most of the observations can be fit at the ~1σ error bars, the 5.8 μm is fit only at ~2.5σ. The dominant source of opacity in this channel comes from H_2O. In the non-inversion scenario, a low water content could potentially explain the lack of absorption in this channel but will overpredict the flux in the 24 μm channel.

4.2. HAT-P-7b

HAT-P-7b is one of the hottest transiting hot Jupiters known. Being the hottest of our sample of planets, it is also the most expected hot Jupiter in our sample to host a thermal inversion. We use the dayside observations of HAT-P-7b reported in four channels of *Spitzer* IRAC photometry by Christiansen et al. (2010). The constraints on the molecular abundances, and departures from equilibrium, for the inversion and non-inversion models are shown in Tables 1 and 2, and Figures 4 and 5.

Our results confirm previous findings that the inversions models fit the observations of HAT-P-7b better than models without thermal inversions. As shown in Figure 4, inversion models can fit the observations to within the 1σ errors (i.e., $\xi^2 \leqslant 1$) for a wide range of methane and CO concentrations, including those close to TE$_\odot$ values. On the other hand, the best-fitting non-inversion model has a $\xi^2 = 1.65$, indicating a fit at 1.3σ errors. Even then, the best-fitting non-inversion models of HAT-P-7b shown in Figure 4 (blue dots) require methane abundances that are over 5 orders of magnitude greater than the TE$_\odot$ values, which are seemingly implausible.

The observations of HAT-P-7b can plausibly be explained without a thermal inversion at the $\xi^2 = 3$ level, i.e., fits at 1.7σ errors (green dots). At this level, models with methane and CO concentrations only marginally deviant from TE$_\odot$ values can explain the data. However, such a degree of fit may not be statistically representative of the true nature of the planet atmosphere. A sample of non-inversion temperature profiles at different levels of fit is shown in Figure 3. The *P*–*T* profiles at $\xi^2 \leqslant 2$ are shown in Figure 3. The brown profiles show the 30 best-fit *P*–*T* profiles below $\xi^2 = 2$.

Two model spectra, corresponding to models with and without a thermal inversion, are shown in Figure 6, along with the corresponding temperature profiles. The model parameters for each case are shown in Table 3. As shown in Figure 6, the non-inversion model is unable to fit the low flux at 3.6 μm and the high flux at 8 μm, simultaneously. The reason for this behavior is
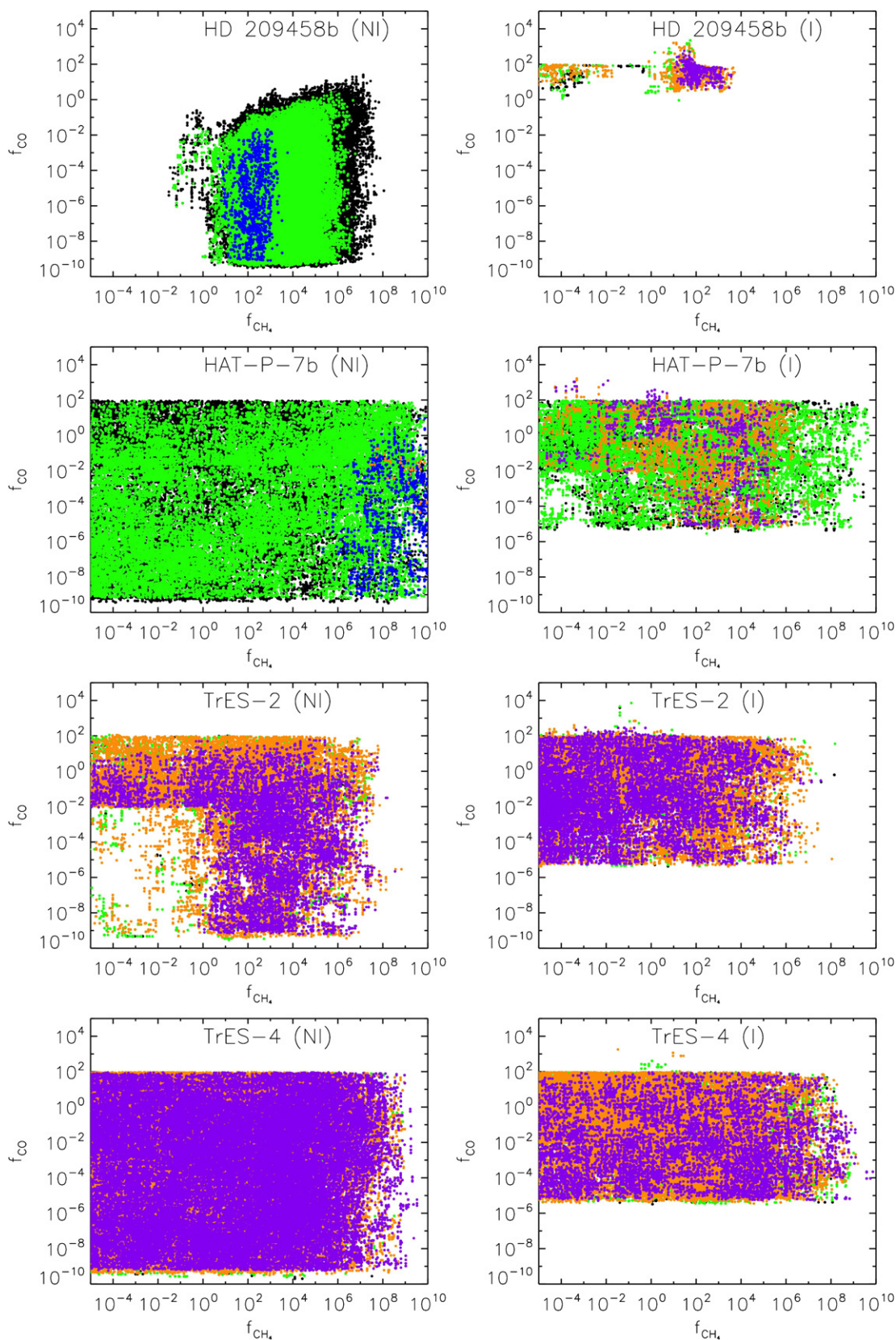
Figure 4. Departures from chemical equilibrium of CH₄ and CO. The dots indicate the regions in the space of CO and CH₄ mixing ratios explored by the MCMC chain (see Section 3.2); each dot is a model realization. All models with C/H and O/H within $(10^{-2}-10^2)$ × solar are shown. The boundaries in the composition space are described in Section 3.2. For each planet, f_{CO} and f_{CH_4} are the departures in the mixing ratios of CO and CH₄ from those corresponding to thermochemical equilibrium with solar abundances (TE$_\odot$) for the same temperature structure (see Section 3.1). For example, $f_{CO} = 1$ implies a CO concentration that is at TE$_\odot$. The left (right) panel for each system shows constraints on models without (with) thermal inversions. Non-inversion and inversion models are labeled with (NI) and (I), respectively. The purple, orange, green, and black colors correspond to $\xi^2 \leqslant 1$, $1 \leqslant \xi^2 \leqslant 2$, $2 \leqslant \xi^2 \leqslant 3$, and $3 \leqslant \xi^2 \leqslant 4$, respectively. The blue dots for non-inversion models in HD 209458b and HAT-P-7b correspond to $2.0 < \xi^2 \leqslant 2.25$; the best-fitting model for HD 209458b has a $\xi^2 = 2.04$, and that for HAT-P-7b has $\xi^2 = 1.65$.
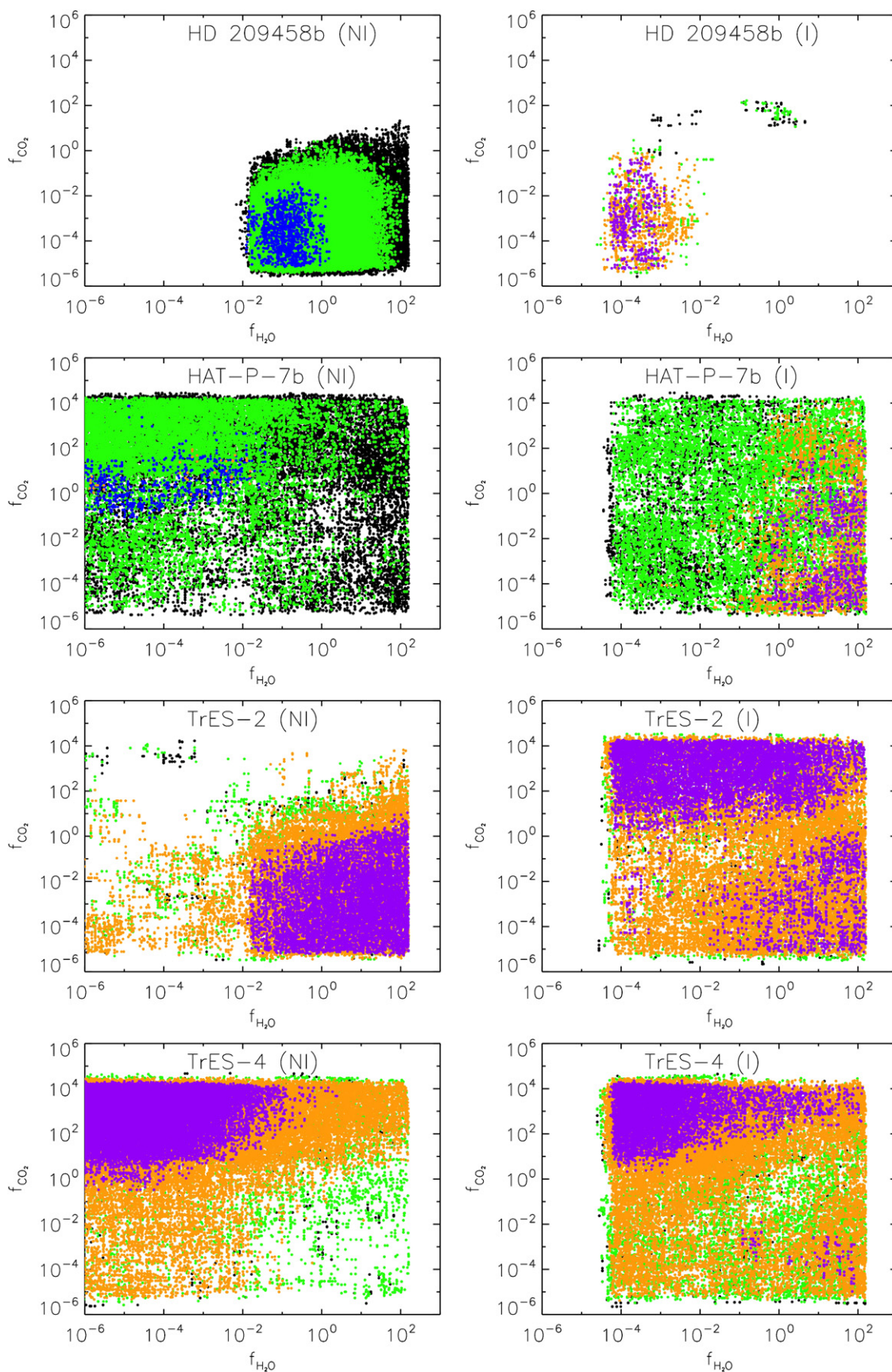
Figure 5. Departures from chemical equilibrium of H_2O and CO_2. For each planet, f_{H_2O} is the departure in H_2O mixing ratio from that corresponding to $TE_\odot$ (see Figure 4), and f_{CO_2} is the departure in CO_2 mixing ratio from a constant value of 10^{-6} (see Section 3.1). The description of panels and colors is identical to that in Figure 4. All models with C/H and O/H within $(10^{-2}–10^2) \times$ solar are shown. The boundaries in the composition space are described in Section 3.2.
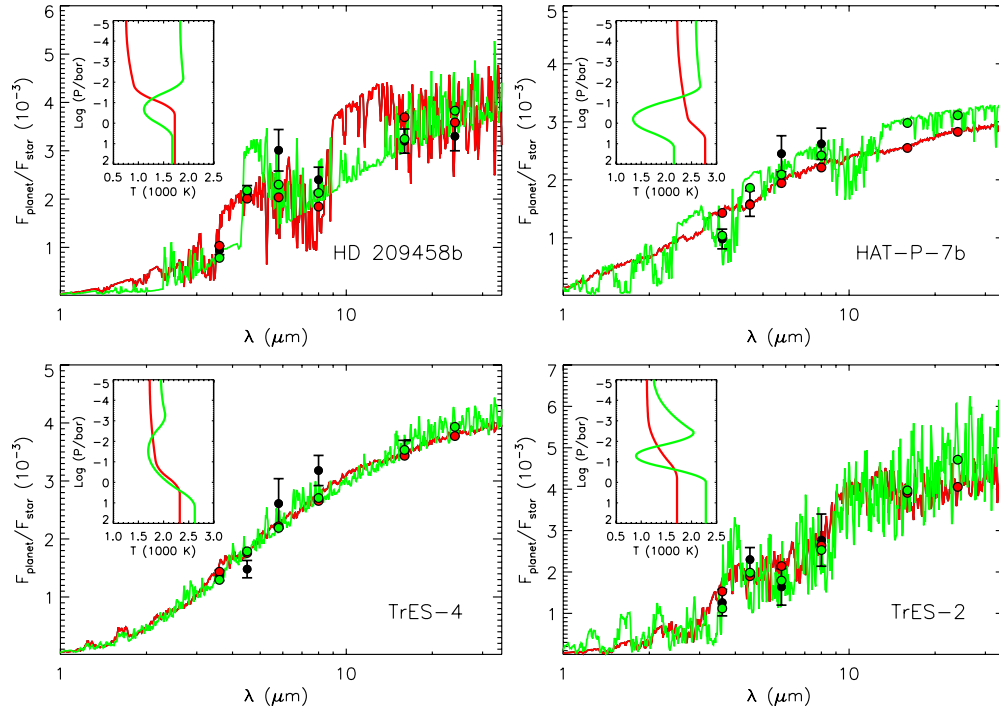
Figure 6. Sample model spectra for each system. Two model spectra, corresponding to models with and without a thermal inversion, are presented for each system. The models represent a balance between degree of fit and physical plausibility. The corresponding P–T profiles are shown in the insets. The atmospheric compositions and day–night redistribution corresponding to each model are shown in Table 3. In each panel, the black circles with error bars (and the upper limit for TrES-4) are the available *Spitzer* observations (see the text for details). The red and green circles are the channel-integrated model spectra in the six *Spitzer* photometric channels, corresponding to the red and green curves, respectively.

(A color version of this figure is available in the online journal.)

because both channels have absorption features due to methane. A low (high) methane concentration in a non-inversion model causes high (low) observed flux in both the channels, contrary to what is observed. On the other hand, the inversion model easily explains all the observations. The low flux in the 3.6 μm channel is explained by the temperature decreasing outward in the lower layers, and the high flux at 8 μm is explained by the high temperatures, due to the thermal inversion, in the higher layers where the contribution to the 8 μm channel peaks.

The day–night redistribution is well-constrained by the data. At the $\xi^2 = 2$ level, the constraint on $\eta = (1 - A)(1 - f_r)$ is 0.7–1.0, for non-inversion models. This range allows for a maximum redistribution of 0.26, assuming zero albedo, and hence implies relatively inefficient advection of energy to the night side. This finding is consistent with the low redistribution of an inversion model reported in Christiansen et al. (2010), and the finding of low redistribution in the visible light curve of *Kepler*. The inversion models on the other hand allow for a wider range of $\eta = 0.41$–0.85 at the $\xi^2 \leqslant 2$ level, allowing for models with efficient day–night redistribution and those otherwise.

In principle, the allowed parameter space of the models can be further restricted by the observation in the visible (centered at 0.63 μm) obtained by the *Kepler Space Telescope* (Borucki et al. 2009). However, modeling the visible flux in the *Kepler* bandpass introduces another five free parameters in terms of the dominant opacity sources in the visible—the atmospheric concentrations of TiO, VO, Na, K, and a prescription for scattering. These five parameters, which are largely decoupled from the opacity sources in the IR, allow a large degree of flexibility in fitting the one *Kepler* observation. By exploring a preliminary range of values for the five parameters, we do find that some of our best-fit non-inversion models for the *Spitzer*

data are also able to fit the *Kepler* point. In an earlier work, we found that the *Kepler* point could also be fit with models with thermal inversions (Christiansen et al. 2010).

4.3. TrES-4

TrES-4 is the second hottest planet in our sample, after HAT-P-7b, and is highly favored to host a thermal inversion, on theoretical grounds (Fortney et al. 2008). We use the five *Spitzer* photometric observations of Knutson et al. (2009), which have been previously reported as evidence for a thermal inversion in TrES-4.

We find that existing observations of TrES-4 can be explained almost equally well by models with and without thermal inversions, contrary to previous findings. Our fits for each case are better than $\xi^2 = 1$, i.e., within the 1σ error bars. The non-inversion P–T profiles fitting the data at the $\xi^2 \leqslant 1$ and $\xi^2 \leqslant 2$ levels are shown in Figure 3.

As shown in Figure 4, non-inversion models can fit the observations of TrES-4 to within $\xi^2 \leqslant 1$, for a wide range of CO and CH$_4$ abundances, including the values at TE$_\odot$, represented by $f_{CO} = 1$ and $f_{CH_4} = 1$. However, we find that the best-fitting models (within $\xi^2 \leqslant 1$) without inversions require a high concentration of CO$_2$, $\gtrsim 10^{-4}$, for TE$_\odot$ concentrations of the remaining molecules like H$_2$O (e.g., Figure 5). This requirement arises from the non-detection of planet flux observed in the 16 μm channel. Since the dominant contribution to this channel comes from the CO$_2$ feature at 15 μm, a non-detection of flux indicates substantial absorption due to CO$_2$ and hence the high CO$_2$ requirement. At the high temperatures of TrES-4, a CO$_2$ concentration of 10^{-4} is not feasible via equilibrium chemistry at solar abundances. However, CO$_2$ concentrations as high as

$\sim 10^{-4}$ are, in principle, feasible for a high metallicity, over $30\times$ solar (Zahnle et al. 2009; Madhusudhan & Seager 2010).

Non-inversion model fits at the $\xi^2 \leqslant 2$ level, on the other hand, do allow for a very plausible set of chemical compositions. Figure 6 shows a model spectrum without a thermal inversion (in red) and having a chemical composition close to $TE_\odot$ (Table 3 shows the composition). Also shown for reference is a model with a thermal inversion. The constraints on the molecular abundances are shown in Tables 1 and 2, for models without and with thermal inversions, respectively. We conclude that the observations place almost no constraints on the molecular concentrations in the atmosphere of TrES-4, in either scenario. While the wide range in allowed chemical compositions is seemingly implausible, it does allow for a significant population of non-inversion models that are physically plausible (see Section 5.2). We find this evidence enough to conclude that there is no sure sign of a thermal inversion in TrES-4, given current data.

4.4. TrES-2

Our results show that the observations of TrES-2 can be explained to a high degree of fit by models both with and without thermal inversions. This general conclusion is similar to that of O'Donovan et al. (2010), where we first reported that the data could be fit by models with and without thermal inversions. In that study, our non-inversion models fitting the data required a CO abundance that was lower than $TE_\odot$ by about 2 orders of magnitude, whereas the best-fit inversion models allowed $TE_\odot$ composition. However, with the new parameter exploration routine, in the present study we have been able to explore regions of parameter space well beyond what we could pursue in O'Donovan et al. (2010). While our present results for inversion models agree with our previous findings, our results for non-inversion models go beyond our findings in O'Donovan et al. (2010).

The best-fit solutions with no thermal inversions in the present study span a wide range in chemical composition, including that of $TE_\odot$. Our results show that the P–T profile is mostly unconstrained by the data, resulting in a large region of parameter space that can explain the observations even at the $\xi^2 = 1$ level. Figure 3 shows the non-inversion P–T profiles corresponding to $\xi^2 \leqslant 1$ and $\xi^2 \leqslant 2$.

The constraints on the atmospheric composition and day–night redistribution are shown in Tables 1 and 2, and in Figures 4 and 5. For each scenario, i.e., with or without a thermal inversion, there is a wide range in molecular composition that can explain the data, including that of thermochemical equilibrium with solar abundances (i.e., $TE_\odot$). The composition in each scenario is practically unconstrained even at the $\xi^2 \leqslant 1$ level. It follows that the C/O ratio is also unconstrained by the data, spanning a rather unphysical range of 5×10^{-5}–4×10^3 even at the $\xi^2 = 1$ level, for the non-inversion models, for example. The large range in C/O is a consequence of allowing the molecular mixing ratios to vary arbitrarily. Nevertheless, it does indicate that best-fit solutions with no thermal inversions can be found at the $\xi^2 \leqslant 1$ level with very plausible molecular concentrations (see Section 5.2), and both carbon-dominated and oxygen-dominated atmospheres are allowed by the observations. Similarly, the day–night redistribution is also unconstrained by the data, at the $\xi^2 = 1$ level.

Based on the existing *Spitzer* IRAC observations, therefore, our results show that a thermal inversion cannot be inferred in the dayside atmosphere of TrES-2. The weak constraints on the

atmosphere of TrES-2 are evident from the data. The flux ratio in the 4.5 μm IRAC channel is noticeably higher than that in the 3.6 μm channel, hinting at a possible emission feature due to a thermal inversion. However, the flux ratio in the 5.8 μm channel is noticeably lower than that in the 8 μm channel allowing for H_2O absorption, and hence the lack of a thermal inversion. Thus, while a model with thermal inversion can explain the data, a thermal inversion is not required by existing IRAC observations of TrES-2. Two best-fit models for TrES-2, with and without a thermal inversion, are shown in Figure 6, and the corresponding compositions are shown in Table 3. The models for both the cases shown here span a rather plausible range of chemical compositions.

5. SUMMARY AND DISCUSSION

We have investigated the question of whether thermal inversions can be robustly inferred from existing *Spitzer* photometric observations of thermal emission from hot Jupiter atmospheres. We addressed this objective by thoroughly exploring the parameter space of models with and without thermal inversions for a sample of four hot Jupiters. We considered four systems which have *Spitzer* observations at four or more wavelengths, and are highly irradiated, so that they are theoretically favored to host thermal inversions (Hubeny et al. 2003; Fortney et al. 2008): HD 209458b, HAT-P-7b, TrES-4, and TrES-2. Furthermore, the observations considered have also been previously reported to be consistent with thermal inversions in the corresponding systems, albeit less robustly. In this work, we addressed to what level of statistical significance and physical plausibility thermal inversions can be inferred in each of these systems.

Our primary finding is that a detailed exploration of the model parameter space is necessary to make robust inferences of thermal inversions in exoplanetary atmospheres. We find that the observations of TrES-4 and TrES-2 can be explained by models with and without thermal inversions, and with physically plausible chemical compositions, at the $\xi^2 \leqslant 2$ and $\xi^2 \leqslant 1$ levels, respectively. This finding is in contrast to the findings of Knutson et al. (2009) and Spiegel & Burrows (2010) who, based on forward models of Burrows et al. (2008), have suggested the requirement of thermal inversion from the same data sets. The difference in conclusions results from the different modeling schemes; the forward models of Burrows et al. (2008) assume layer-by-layer radiative equilibrium and chemical equilibrium, and a parameterization for day–night energy redistribution. On the other hand, for a given data set, we explore the space of temperature profile and composition, without the requirement of layer-by-layer radiative equilibrium or chemical equilibrium, but still imposing the strict constraint of global energy balance. We note that our best-fitting inversion solutions for TrES-2 and TrES-4 do include a wide range of profiles with thermal inversions, which likely encompass the profiles of Knutson et al. (2008) and Spiegel & Burrows (2010). Another interesting result is that if TrES-4 indeed does not host a thermal inversion, the best-fitting non-inversion solutions require a large CO_2 mixing ratio ($\geqslant 10^{-5}$), which might be an indication of enhanced metallicity in TrES-4 (Zahnle et al. 2009; Madhusudhan & Seager 2010).

For HD 209458b and HAT-P-7b, we find that the observations cannot be explained without thermal inversions to within a $\xi^2 < 3$, i.e., to within 1.7σ observational uncertainties, for any plausible composition. Any better fit would require substantial enhancements in methane and depletion of CO, which is implausible at the high temperatures in the systems considered.

Our inference of thermal inversions in HD 209458b and HAT-P-7b is consistent with previous findings of Burrows et al. (2008), Knutson et al. (2008), Christiansen et al. (2010), and Spiegel & Burrows (2010). Our results show that a detailed exploration of the model parameter space and an accurate assessment of the observational errors are essential to robustly infer thermal inversions based on existing photometric observations. For example, if one considers the 2σ error bars on the data, thermal inversions may not be required even for compositions in chemical equilibrium.

5.1. Thermal Inversions or Not?

Whether or not the observations considered in this work can be explained without a thermal inversion depends on what level of fit, and physical plausibility of models, one is willing to consider. If we do not consider the physical plausibility of the best-fit models, the observations of all four hot Jupiters can be explained without thermal inversions to within the 1.5σ error bars, i.e., $\xi^2 \leqslant 2.25$. On the other hand, if we consider only models fitting within the 1σ error bars, and/or enforce arguments of physical plausibility (see Section 5.2 below), HAT-P-7b and HD 209458b emerge as likely to host thermal inversions. The inference of a thermal inversion is, therefore, very sensitive to the reported observational uncertainties.

The inference of a thermal inversion can also be sensitive to one data point over others. In HD 209458b, for instance, several of the six observations can be fit at the $\sim 1\sigma$ error bars by non-inversion models (e.g., Figure 6). A large contribution to the ξ^2 comes predominantly from the 5.8 μm point which is fit only at greater than 2σ. Thus, for these models it is only the 5.8 μm IRAC point which guides any inference we make about thermal inversions. Similarly, for the model spectra shown for HAT-P-7b, the dominant contribution to ξ^2 comes from the 8 μm IRAC point. Therefore, any inference of thermal inversions can be highly sensitive to the reported observational uncertainties in a single channel, which varies on a case by case basis.

At the level of current observations, our results potentially deviate from theory. Given that the atmospheres of TrES-4 and TrES-2 can be explained by models without thermal inversions, it is possible that these systems do not host thermal inversions. If that happens to be the case, the results are in contrast to theoretical predictions, as both TrES-4 and TrES-2 have higher levels of incident star flux as compared to HD 209458b (Fortney et al. 2008), and hence are more likely to host thermal inversions. Nevertheless, since the observations for these systems are consistent with models both with and without thermal inversions, the only conclusion is that it is too early to claim thermal inversions in these systems, contrary to some previous studies.

5.2. Plausibility of Models

An important point concerns the physical plausibility of non-inversion models fitting the observations. As shown in Figure 4, the best-fit non-inversion models for HD 209458b and HAT-P-7b require substantial enhancement of CH_4 as compared to CO. However, as explained in Section 2.3, in the very hot atmospheres of these planets, CO is expected to be the dominant molecule, based on atmospheric chemistry. We currently do not have a physically plausible explanation for such CH_4 enhancement at the expense of CO in a very hot atmosphere.

Our best-fit models explore an unrestricted range of atmospheric compositions. In trying to conduct an unbiased exploration of the parameter space, we have allowed for all the

molecules to vary over a large range of values that might be seemingly unphysical. For example, in TrES-2 the $\xi^2 = 1$ limits extend to mixing ratios as high as 0.1 for H_2O, CO, and CH_4. Such high mixing ratios indicate extreme metallicities that are too high to be plausible, although not impossible. For reference, solar abundances have number fractions of C and O at 3.3×10^{-4} and 7.8×10^{-4}, respectively (Anders & Grevesse 1989; used in equilibrium chemistry calculations of Burrows & Sharp 1999; but cf., Allende Prieto et al. 2002; Asplund et al. 2005, for recent values which are lower by a factor of ~ 2). Similarly, for HAT-P-7b and TrES-2 the C/O ratios span many orders of magnitude reaching values as high as 10^4, which are also manifestly unphysical. For instance, the solar C/O ratio is ~ 0.5. However, the best-fitting models, with and/or without inversions, for all the systems do allow C/O ratios in the plausible range of 0.1–1.

Finally, we have not explored the realm of drastically inhomogeneous models—those models where the mixing ratio of a molecule could be very different in different layers of the atmosphere. It is understandable that photochemistry and vertical mixing can deviate molecular mixing ratios away from equilibrium (e.g., Line et al. 2010; Madhusudhan & Seager 2010). We expect that our prescription for molecular species, which is parameterized as deviations from chemical equilibrium, spans the space of possible deviations. However, we have not considered arbitrarily populating different layers of the atmosphere with different species. Ad hoc filling of the layers with specific molecules might allow a large, albeit unphysical, degree of freedom in fitting the observations.

5.3. Future Observations to Resolve the Degeneracy

In this work, we have addressed the apparent degeneracy between atmospheric composition and thermal inversions in hot Jupiter atmospheres. The large number of model parameters allows the freedom to fit the limited observations of some atmospheres in any scenario, i.e., with or without inversions; although at different levels of fit. Future developments in observations and theory are needed to break the apparent degeneracies. Theoretical efforts are needed to put limits of physical plausibility on the atmospheric composition and temperature structure. Such limits, for example, might exclude many of the non-inversion models that fit the observations considered in this work.

New observations are important for better constraints on thermal inversions. In the near future, multiple observations of thermal emission from transiting hot Jupiters in the near-IR, from the ground and with the *HST*, along with existing *Spitzer* data can help constrain models to a good extent, on a case-by-case basis. For instance, the two model spectra of HAT-P-7b in Figure 6 show only modest differences in the *Spitzer* bandpasses. However, the spectra are markedly different in the near-IR, especially in the continua between the molecular features, which can potentially be observed from ground, e.g., in the *J*, *H*, and *K* bands. Additional constraints can be also placed by observations within the molecular features, which are possible with space-based observations (e.g., with the *HST*), except for molecules like methane where ground-based observations might also be feasible. Near-IR observations have been reported for a few systems to date, not particularly constraining thermal inversions (e.g., Swain et al. 2009; Croll et al. 2010). However, multi-band near-IR photometry and/or spectroscopy can prove to be a rich resource for targeted searches for thermal inversions in exoplanetary atmospheres. Targets can be selected based on constraints from already

existing *Spitzer* observations, irradiation levels, and sensitivity of a given instrument to the planet–star flux contrasts. The several near-IR bandpasses mentioned above are currently ripe for this purpose. In the long run, high-resolution spectra with the *James Webb Space Telescope* will have the sensitivity to conclusively identify the presence of thermal inversions based on spectrally resolved emission features.

An important point concerns the opportunity to observe in the two IRAC channels on *Warm Spitzer*. While it is true that robust inferences of thermal inversions could not be made even with four *Spitzer* points in several known cases, a large difference between the 3.6 μm and 4.5 μm channels can place stringent constraints on the existence of thermal inversions. A very large flux excess in the 4.5 μm channel over the 3.6 μm channel is highly indicative of a thermal inversion, although it also depends on the irradiation level of the planet which governs the blackbody continuum. A large excess in the 3.6 μm channel, on the other hand, is almost a sure sign of no thermal inversion, as in the cases of HD 189733b (Madhusudhan & Seager 2009) and GJ 436b (Stevenson et al. 2010; Madhusudhan & Seager 2010). Thus, observations of hot Jupiters with *Warm Spitzer* would likely be able to identify the extreme cases of systems with or without thermal inversions.

Tremendous progress has been made in the last decade in our understanding of exoplanetary atmospheres. At the same time, recent and current observations allow us a chance to revisit previous interpretations made with limited observations. It is now upon us to evaluate all the theoretical options and observational uncertainties so as to determine a framework in which to interpret observations. Judicious target selection and efficient planning of future observations, from ground and from space, will be critical to characterizing the atmospheres of the growing number of transiting exoplanets.

REFERENCES

Allende Prieto, C., Lambert, D. L., & Asplund, M. 2002, ApJ, 573, L137
Anders, E., & Grevesse, N. 1989, Geochim. Cosmochim. Acta, 53, 197
Asplund, M., Grevesse, N., & Sauval, A. J. 2005, in ASP Conf. Ser. 336, Cosmic Abundances as Records of Stellar Evolution and Nucleosynthesis, ed. T. G. Barnes, III & F. N. Bash (San Francisco, CA: ASP), 25
Barman, T. S., Hauschildt, P. H., & Allard, F. 2005, ApJ, 632, 1132
Borucki, W. J., et al. 2009, Science, 325, 709
Borysow, A. 2002, A&A, 390, 779
Borysow, A., Jorgensen, U. G., & Zheng, C. 1997, A&A, 324, 185
Burrows, A., Budaj, J., & Hubeny, I. 2008, ApJ, 678, 1436
Burrows, A., Hubeny, I., Budaj, J., Knutson, H. A., & Charbonneau, D. 2007, ApJ, 668, L171
Burrows, A., & Sharp, C. M. 1999, ApJ, 512, 843
Castelli, F., & Kurucz, R. L. 2004, arXiv:astro-ph/0405087v1 (ftp://ftp.stsci.edu/cdbs/grid/ck04models/)
Chamberlain, J. W. 1978, Theory of Planetary Atmospheres (New York: Academic)
Christiansen, J., et al. 2010, ApJ, 710, 97
Cooper, C. S., & Showman, A. P. 2006, ApJ, 649, 1048
Croll, B., et al. 2010, ApJ, 717, 1084
Deming, D., Seager, S., Richardson, L. J., & Harrington, J. 2005, Nature, 434, 740
Ford, E. 2005, ApJ, 129, 1706
Fortney, J. J., Lodders, K., Marley, M. S., & Freedman, R. S. 2008, ApJ, 678, 1419
Fortney, J. J., Saumon, D., Marley, M. S., Lodders, K., & Freedman, R. S. 2006, ApJ, 642, 495
Freedman, R. S., Marley, M. S., & Lodders, K. 2008, ApJS, 174, 504
Fressin, F., Knutson, H. A., Charbonneau, D., O'Donovan, F. T., Burrows, A., Deming, D., Mandushev, G., & Spiegel, D. 2010, ApJ, 711, 374
Gilks, W. R., Richardson, S., & Spiegelhalter, D. J. 1998, Markov Chain Monte Carlo in Practice (Boca Raton, FL: Chapman and Hall/CRC)
Hubeny, I., Burrows, A., & Sudarsky, D. 2003, ApJ, 594, 1011
Knutson, H. A., Charbonneau, D., Allen, L. E., Burrows, A., & Megeath, S. T. 2008, ApJ, 673, 526
Knutson, H. A., Charbonneau, D., Burrows, A., O'Donovan, F. T., & Mandushev, G. 2009, ApJ, 691, 866
Knutson, H. A., Howard, A. W., & Isaacson, H. 2010, ApJ, 720, 1569
Liang, M-C, Parkinson, C. D., Lee, A. Y.-T., Yung, Y. L., & Seager, S. 2003, ApJ, 596, L247
Line, M. R., Liang, M.-C., & Yung, Y. L. 2010, ApJ, 717, 496
Machalek, P., McCullough, P. R., Burrows, A., Burke, C. J., Hora, J. L., & Johns-Krull, C. M. 2009, ApJ, 701, 51
Madhusudhan, N., & Seager, S. 2009, ApJ, 707, 24
Madhusudhan, N., & Seager, S. 2010, ApJ, 722, 871
O'Donovan, F. T., Charbonneau, D., Harrington, J., Madhusudhan, N., Seager, S., Deming, D., & Knutson, H. A. 2010, ApJ, 710, 1551
Rothman, L. S., et al. 2005, J. Quant. Spectrosc. Radiat. Transfer, 96, 139
Seager, S., Richardson, L. J., Hansen, B. M. S., Menou, K., Cho, J. Y.-K., & Deming, D. 2005, ApJ, 632, 1122
Showman, A. P., Fortney, J. J., Lian, Y., Marley, M. S., Freedman, R. S., Knutson, H. A., & Charbonneau, D. 2009, ApJ, 699, 564
Spiegel, D. S., & Burrows, A. 2010, ApJ, 722, 871
Spiegel, D. S., Silverio, K., & Burrows, A. 2009, ApJ, 699, 1487
Stevenson, K., et al. 2010, Nature, 464, 1161
Swain, M. R., et al. 2009, ApJ, 704, 1616
Tegmark, et al. 2004, Phys. Rev. D, 69, 103501
Zahnle, K., Marley, M. S., Lodders, K., & Fortney, J. J. 2009, ApJ, 701, L20